Materials & Design 235 (2023) 112409

Contents lists available at ScienceDirect

Materials & Design

journal homepage: www.elsevier.com/locate/matdes

Electrical tree modelling in dielectric polymers using a phase-field regularized cohesive zone model

Qi Wang [a], Yuheng Deng [b], Malvern Yap [a], Yan Yang [a], Jielin Ma [a], Wen Kwang Chern [a,c], Jin Li [d], Zhong Chen [a,b,*]

[a] SP Group – NTU Joint Laboratory, School of Electrical and Electronic Engineering, Nanyang Technological University, 50 Nanyang Avenue, 639798, Singapore
[b] School of Materials Science and Engineering, Nanyang Technological University, 50 Nanyang Avenue, 639798, Singapore
[c] Singapore Power Group, 349277, Singapore
[d] Key Laboratory of Smart Grid of Education Ministry, School of Electrical and Information Engineering, Tianjin University, Tianjin 300072, China

ARTICLE INFO

Keywords:
Electrical treeing
Phase field
Weibull distribution
Dielectric polymers
Dielectric breakdown

ABSTRACT

Electrical treeing is a leading cause to the eventual breakdown of dielectric polymers under high voltages. This paper presents a simulation scheme developed based on the phase-field regularized cohesive zone model (PF-CZM) for electrical tree modelling. By using the electrical analog of the crack propagation, the localized breakdown is modelled by the evolution of surface energy, and the electrical treeing is driven by the competition between the surface energy and the stored energy following the laws of thermodynamics. The microscopic Weibull distribution of the dielectric breakdown strength is the key factor resulting in the fractal structures of the electrical tree. The model developed is mesh independent and length-scale insensitive when the mesh size is no greater than 2.5μm. The validity of the model was confirmed through experiments, which strengthens its credibility. Three types of composites are designed and compared. The results indicate that the epoxy resin enhanced with 5 vol% silica and 1 vol% graphene sheet has a 3.5 % longer dielectric breakdown time and a 29.2 % higher thermal conductivity than the pure epoxy resin. Overall, the model provides a valuable tool for understanding the physics of electrical treeing and designing new dielectric materials with high withstand voltages.

1. Introduction

The prominence of global industrialization and the resultant global environmental issues has made carbon neutrality an essential part of global climate governance [1]. For this purpose, high-performance energy-storage and transmission techniques have gained more attention. High-voltage dielectric polymers and its composites play an extremely important role in these techniques as the device components are usually operated under high-voltage conditions [2–7]. Dielectric breakdown often occurs when the dielectric polymers is in operation, limiting their applications [8]. Electrical treeing, caused by existing defects such as voids and impurities, is one of the major mechanisms that leads to breakdown in dielectric polymers when subjected to high voltages [9–11]. The localized high electric field caused by these defects can cause electrical trees to grow. The growth of the tree-like micro-channels is driven by partial discharges (PD), accompanied by impulse thermal or impulse mechanical breakdown [11]. Eventually, the dielectric breakdown occurs due to the formation of the conductive channels in the material.

For the past several decades, numerous numerical models have been proposed to understand the electrical treeing mechanism [12–15]. The stochastic NPW (Niemeyer-Pietronero-Wiesmann) model was among the first attempts to model the fractal structure of the electrical tree [12]. In this model, the tree structures grow discretely, and the probability of the extension is proportional to the power η of the local electric field along the possible extension paths on the two-dimensional square lattice. The model can generate similar tree structures to those observed experimentally with controllable fractal dimension. However, the predicted structure of the stochastic model is highly sensitive to the value of power η, which cannot be related to a specific physical process. The DAM (Discharge-Avalanche Model) is another popular electrical tree simulation model, in which the tree propagation is assumed to be caused by the electron avalanches along their path on a 2-D square lattice per unit step time [13]. However, some parameters in this model, such as the

* Corresponding author at: SP Group – NTU Joint Laboratory, School of Electrical and Electronic Engineering, Nanyang Technological University, 50 Nanyang Avenue, 639798, Singapore.
E-mail address: aszchen@ntu.edu.sg (Z. Chen).

https://doi.org/10.1016/j.matdes.2023.112409
Received 9 March 2023; Received in revised form 12 October 2023; Accepted 16 October 2023
Available online 18 October 2023

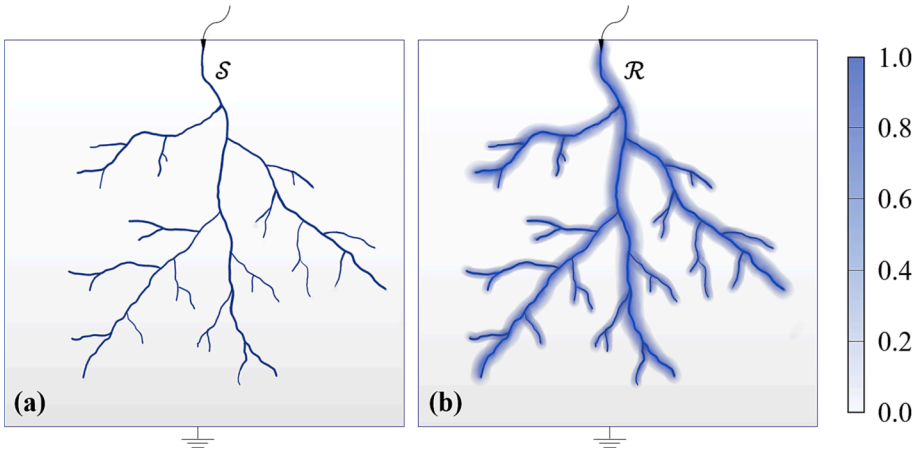

Fig. 1. Illustration of the geometric regularization of the sharp dielectric damage pattern. (a) A sharp dielectric damage. (b) A geometrically regularized dielectric damage.

fractal dimension and the characteristic time, are difficult to be determined in practice, limiting the ability of this model to explain the mechanisms behind the discharge phenomena.

The above models did not rely on Maxwell's equations when modelling the treeing structures. Instead, the stochastic disturbances are introduced about the local electrostatic field as a seed for branching [14]. To quantitively discuss the discharge phenomena while considering the electromagnetic field variables, Noguchi et al. [14] proposed a finite element analysis (FEA) model to simulate the dielectric breakdown based on Maxwell's equations, in which the breakdown was expressed as the local change of conductivity. This model has a major drawback in that the breakdown criterion is based on the critical value of the norm of electric fields, while the energy-based criterion is more realistic. Moreover, the model requires dual sets of geometries, the Delaunay tessellation and the Voronoi tessellation, to discretize Maxwell's system. This has increased the model complexity. Xia et al. [16] developed a thermodynamic framework to simulate the evolution of dielectric damage with respect to the electric field. The form of the dissipation potential for the dielectric damage is taken from mechanical damage potential.

The dielectric breakdown is a localized damage process that can be recognized as the electrical analogue of crack propagation in solids [17]. The theory of linear elastic fracture mechanics (LEFM), a topic in the subject of elastic fracture, is well developed based on the milestone work of Griffith [18]. Various computational models have been proposed, such as the phase-field model (PFM) [19–24], peridynamics [25,26], cracking particles method [27–29], etc. Inspired by the similarity between dielectric breakdown and mechanical breakdown in the form of a brittle fracture, the PFM was introduced to simulate the electrical treeing and dielectric breakdown in recent years [2,30–35]. The PFM models the systems with sharp interfaces using a continuous phase-field variable that differentiates between multiple physical phases through a smooth transition [36]. An attractive advantage of the PFM is its ability to simulate crack nucleation, propagation, merging, and branching, purely based on energy minimization without additional ad-hoc criteria [37]. The crack propagation is automatically tracked by the evolution of the smooth phase field without the need to track the forepart of the crack. Meanwhile, compared to other computational techniques, PFM has the advantages of continuous representation of crack damage, ease of coupling with other physical phenomena. (Please refer to [38–40] for more details on the abovementioned methods).

Shen et al. [32] developed a phase-field model to investigate the breakdown behaviour of polymer nanocomposites. Using this model, a sandwich-structured nanocomposite with higher energy density was designed. The phase-field model was further enhanced with multi-physics condition considered [31], and combined with machine learning to accelerate the simulation [30]. Zhu et al. [33] further developed the phase-field model by Shen et al. [32] by setting the parameter to be time- and position-dependent to produce the fractal electrical tree structure in nanocomposites. Cai et al. [2] simulated the electrical tree propagation in a parallel capacitor and a cylindrical capacitor by a phase-field model. The factors affecting the treeing morphology and the effect of fillers on electrical treeing were also discussed using the model.

The abovementioned PFMs are derived dominantly from the Ginzburg-Landau equation [41]. These models are unrelated to Griffith's theory for the fracture toughness does not enter the corresponding equations [36]. The Ginzburg-Landau double-well function in the energy functional used in these models makes it difficult to interpret the Γ-convergence results [42,43]. Furthermore, some parameters, such as the gradient energy coefficient and energy barrier coefficient, can hardly be determined for different materials, which has limited these models' validation when comparing with experimental observations. On the other hand, the implementation of the stochastic nature of dielectric breakdown in the current models is not convincing due to the lack of theoretical rationale.

Analogue to the computational fracture mechanics, this paper aims to develop a novel phase-field model to investigate the mechanism of electrical treeing based on the phase-field regularized cohesive model (PF-CZM) [44,45]. The dielectric breakdown is modelled as the competition between the electric energy stored in the bulk material and the surface energy for electrical tree propagation. The microscopic stochastic distribution of the dielectric breakdown strength is considered the key reason behind the fractal structures of the electrical trees. In the current work, such stochastic distribution is integrated in the model. The model parameters are characterized, and the analyses of mesh sensitivity and length-scale parameter sensitivity are conducted. Finally, the electrical treeing process is investigated, and three types of dielectric composites are designed and compared utilizing the newly developed model.

2. Theoretical model

2.1. Phase-field regularization

To avoid the explicit modelling of sharp damage morphology, the phase-field method smears the sharp damage into a localization band with the phase-field variable [21,22,46]. The damage phase-field variable is defined as [45]:

$$d(\boldsymbol{x}) := \left\{ d | d(\boldsymbol{x}) \in [0,1], \dot{d}(\boldsymbol{x}) \geq 0 \forall \boldsymbol{x} \in \mathscr{R}, d(\boldsymbol{x}) = 1 \forall \boldsymbol{x} \in \mathscr{S} \right\} \tag{1}$$

where $\boldsymbol{x}$ is spatial coordinates, $\mathscr{R}$ is the regularized damage domain around the sharp damage domain $\mathscr{S}$, $\dot{()}$ represents the derivative of time. Considering a two-dimensional case as an example, Fig. 1 illustrates the phase-field regularized dielectric breakdown damage.

With the help of the above defined phase field $d(\boldsymbol{x})$, the sharp damage topology $\Gamma_{\mathscr{S}}$ can be regularized as [44–46]:

$$\Gamma_{\mathscr{S}} = \int_{\mathscr{S}} \mathrm{d}A \approx \int_{\mathscr{R}} \rho(d, \nabla d)\, \mathrm{d}V = \Gamma_{\mathscr{R}}(d) \tag{2}$$

where $\rho(d, \nabla d)$ is the damage surface density functional that approximates the sharp damage surface $\Gamma_{\mathscr{S}}$ with ∇d representing the spatial gradient of the phase-field d, $\Gamma_{\mathscr{R}}$ is a regularized functional. According to the unified phase-field theory, the damage surface density functional is expressed as [45]:

$$\rho(d, \nabla d) = c_\alpha \left[\frac{1}{l} \alpha(d) + l |\nabla d|^2 \right] \tag{3}$$

where $c_\alpha = 4 \int_0^1 \sqrt{\alpha(\beta)}\mathrm{d}\beta$ is the scaling constant, l is the length-scale parameter characterizing the regularized damage band, $\alpha(d)$ is the geometric function which characterize the homogeneous evolution of the phase-field. To ensure that the regularized functional $\Gamma_{\mathscr{R}}(d)$ is zero for the intact state ($d(\boldsymbol{x}) = 0$), and $\Gamma_{\mathscr{R}}(d)$ represents the sharp damage surface $\Gamma_{\mathscr{S}}$ for the fully breakdown state ($d(\boldsymbol{x}) = 1$), $\alpha(d)$ should satisfy $\partial\alpha/\partial d \geq 0$, $\alpha(0) = 0$ and $\alpha(1) = 1$. In this paper, a second-order polynomial function was selected for $\alpha(d)$:

$$\alpha(d) = 2d - d^2 \tag{4}$$

When l approaches zero, the Γ-convergence is satisfied [45,47]:

$$\Gamma_{\mathscr{S}} = \lim_{l \to 0} \Gamma_{\mathscr{R}}(d) \tag{5}$$

It is worth noting that despite the double-well function ($\alpha(d) = d^2(1-d)^2$), which is popular in the physics community, satisfying the properties of $\alpha(0) = \alpha(1) = 0$, it does not satisfy the property of $\partial\alpha/\partial d \geq 0$. The equivalence between the intact state ($d(\boldsymbol{x}) = 0$) and the breakdown state ($d(\boldsymbol{x}) = 1$) likely leads to the damage propagating in the incorrect directions [48].

2.2. Breakdown damage evolution

The breakdown process is irreversible, thus the evolution of the breakdown damage is energy dissipative. With the damage regularization of Eq. (2), the damage surface energy is defined as [44–46]:

$$U_d(\boldsymbol{x}, d) = \int_{\mathscr{S}} G_f \mathrm{d}A \approx \int_{\mathscr{R}} G_f \rho(d, \nabla d) \mathrm{d}V \tag{6}$$

where G_f is the fracture energy per unit damage area. The variation of damage surface energy is derived as:

$$\delta U_d = \int_{\mathscr{R}} G_f \delta\rho \mathrm{d}V \tag{7}$$

The global stored energy functional with respect to the phase-field $d(\boldsymbol{x})$ and the electric field intensity $\boldsymbol{E}(\boldsymbol{x})$ of a dielectric solid body Ω under the electric field is expressed as:

$$U_S(\boldsymbol{E}, d) = \int_\Omega W_e(\boldsymbol{E}, d)\, \mathrm{d}V = \int_\Omega \omega(d) W_{e0}(\boldsymbol{E}, d) \mathrm{d}V \tag{8}$$

where $W_e(\boldsymbol{E}, d)$ is the free energy density functional, $W_{e0}(\boldsymbol{E}, d)$ is the initial electric energy density, $\omega(d)$ is a monotonically decreasing function characterizing the energy degradation of the material during the breakdown process.

The variation of the stored energy functional is derived as:

$$\delta U_S = \int_\Omega \left(\frac{\partial W_e}{\partial \boldsymbol{E}} \bullet \delta \boldsymbol{E} + \frac{\partial W_e}{\partial d} \delta d \right) \mathrm{d}V \tag{9}$$

According to the laws of thermodynamics, the evolution of the damage phase-field should satisfy the following inequality:

$$\delta U_d = \delta U_e - \delta U_S \geq 0 \tag{10}$$

where δU_e is the external virtual power.

2.3. Constitutive and governing equations

The initial electric energy density $W_{e0}(\boldsymbol{E}, d)$ is expressed as:

$$W_{e0}(\boldsymbol{E}, d) = \frac{1}{2\varepsilon} \boldsymbol{D}^2 = \frac{1}{2} \varepsilon \boldsymbol{E}^2, \varepsilon = \varepsilon_0 \varepsilon_r \tag{11}$$

where $\boldsymbol{D}$ and $\boldsymbol{E}$ are the electric displacement field and electric field, respectively. ε is the permittivity of the intact material, $\varepsilon_0 = 8.854 \times 10^{-12}\mathrm{C}/(\mathrm{V} \bullet \mathrm{m})$ is the vacuum permittivity, and ε_r is the relative permittivity.

According to the constitutive law of the dielectric solid, we have:

$$\boldsymbol{E} = \frac{\boldsymbol{D}}{\varepsilon} \tag{12}$$

$$\boldsymbol{E} = \frac{\partial W_e}{\partial \boldsymbol{D}} = \omega(d) \frac{\partial W_{e0}}{\partial \boldsymbol{D}} \tag{13}$$

With respect to the variation of the energy dissipation Eq. (7) and the stored energy Eq. (9), it can be derived from the thermodynamics laws Eq. (10) that:

$$\int_\Omega \left[G_f \delta\rho + \omega'(d) W_{e0} \right] \mathrm{d}V = 0 \text{and} \int_\Omega \left(\frac{\partial W_e}{\partial \boldsymbol{E}} \bullet \delta \boldsymbol{E} \right) \mathrm{d}V = \delta U_e \tag{14}$$

The above equations give the governing equation of the evolution of the damage phase-field in weak form. Subsequently, the strong form can be given as [44]:

$$\begin{cases} -\omega'(d) W_{e0} - G_f \delta_d \rho = 0, \delta d > 0 \\ -\omega'(d) W_{e0} - G_f \delta_d \rho < 0, \delta d = 0 \end{cases} \tag{15}$$

where $\delta_d\rho$ is the variational derivative of the damage surface density expressed as [45]:

$$\delta_d \rho = \frac{1}{c_\alpha} \left[\frac{1}{l} \alpha'(d) - 2l\Delta d \right] \tag{16}$$

To avoid the existing damage recovery after the local electric field decreases, a history state variable H, which drives the evolution of the breakdown damage phase field, is introduced [20,49]:

$$H = \max \left(Y_c, \max_{\tau \in (0,t)} Y_\tau \right) \tag{17}$$

where Y_τ is the electric energy density at the time τ, and Y_c is the critical breakdown energy density, which is critical for the initiation of the breakdown damage as expressed in following:

$$Y_c = \frac{1}{2} \varepsilon_0 \varepsilon_r \overline{E}_b^2 \tag{18}$$

where $\overline{E}_b$ is the nominal dielectric breakdown strength.

The dielectric polymers should prevent electrical conduction under the ideal conditions. However, low-level conduction is often inevitable at high fields [50]. Therefore, coupled with the law of charge conservation, the governing equations for the dielectric breakdown damage phase-field model are given as:

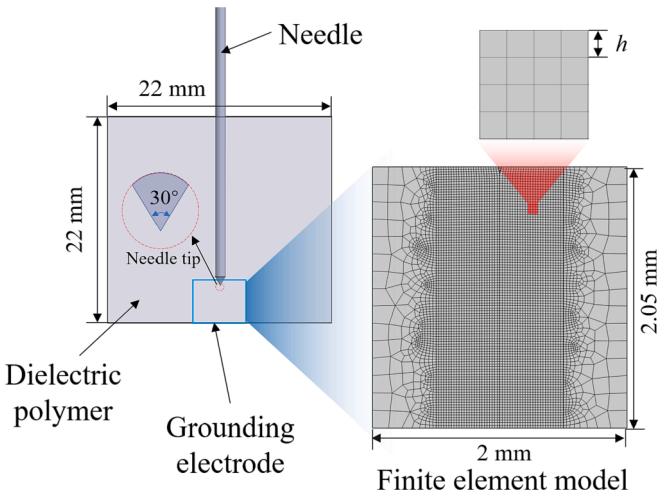

Fig. 2. Dimensions of the finite element model.

$$\begin{cases} \nabla \bullet J + \dfrac{\partial q}{\partial t} = 0 \\ -\omega^{'}(d)H - G_f \delta_d \rho = 0 \end{cases} \tag{19}$$

where $\boldsymbol{J} = \sigma \boldsymbol{E} = -\sigma \nabla V$ is the electric current density, with σ being the electrical conductivity. $\boldsymbol{E}$ and V are the electric field and the electric potential, respectively.

The above governing equations achieve the following Neumann boundary conditions:

$$\begin{cases} E \bullet n = E_m on \partial\Omega_m \\ \nabla d \bullet n = 0 on \partial\Omega \end{cases} \tag{20}$$

with Ω_m the boundary of the electrode and $\boldsymbol{n}$ the outward unit normal vector of the boundary.

Meantime, the following initial conditions will be fulfilled:

$$\begin{cases} V(\boldsymbol{x}, t = 0) = V_0(x) \\ d(x, t = 0) = d_0(x) \end{cases} \tag{21}$$

where the initial phase-field variable $d_0(\boldsymbol{x})$ can be used to model pre-existing breakdown damage by setting $d_0(\boldsymbol{x}) = 1$ locally.

2.4. Degradation function

The degradation function characterizes the deterioration of the stored energy functional with respect to the damage phase-field. There are multiple popular degradation functions used in phase-field modelling. They should have the properties of [20,43]:

$$\begin{cases} \omega^{'}(d) < 0 \\ \omega(0) = 1 \\ \omega(1) = 0 \\ \omega^{'(1)} = 0 \end{cases} \tag{22}$$

In this paper, the following degradation function is employed in accordance with Wu [45]:

$$\omega(d) = \frac{(1-d)^2}{(1-d)^2 + a_1 d \bullet (1 - 0.5d)} \tag{23}$$

where $a_1 = 4G_f / (\pi \varepsilon_0 \varepsilon_r E_b^2 l)$.

3. Numerical implementation

The governing equations presented in Section 2 are implemented in the finite element analysis (FEA) software COMSOL Multiphysics 6.0. The PDE interface, ODE and DAE interface, and the AC/DC module are coupled to solve the phase-field variable, history state variable and the electric potential, respectively. A needle-plane configuration is considered in this study. To save computational cost, a 2-D area from the needle tip to the plane electrode is extracted as the computational domain. Furthermore, the whole computational domain is divided into two sub-domains of which the electrical trees are expected to grow in the central sub-domain, whose element size is small enough to guarantee an accurate estimation of the fracture energy. The dimension of the model is shown in Fig. 2.

The staggered algorithm, which proved to be robust, was employed to solve the nonlinear algebraic governing equations [51] (as depicted in the flow chart of Supplementary Fig. 1). For each new time step, the initial values of the variables are set based on the results solved in the previous solution. Then, the electric potential, ϕ_i^{j+1}, for the given time step i and iteration step $j+1$ is solved by the Newton-Raphson method with respect to the results of the previous iteration [52]. Subsequently, the history state variable H_i^{j+1} is solved with the updated electric potential ϕ_i^{j+1}. The phase-field variable d_i^{j+1} is then obtained with ϕ_i^{j+1} and H_i^{j+1}. The convergence criterion is verified to ensure that the error is within the tolerance requirement. If the convergence criterion is not satisfied, the calculation will go through another round of iteration. Else, the calculation will move to the next time step until the calculation is completed.

4. Parameters characterization

4.1. Dielectric breakdown strength

Dielectric breakdown strength is one of the most critical parameters in this model. It was found that the breakdown test results vary with test specimens under the same testing conditions; therefore, the breakdown strength data should be more appropriately presented as a statistical distribution. Although the Normal distribution is well known and its parameters are easily calculated, it is not usually suitable for electrical breakdown data. The Weibull distribution, which is built on the weakest link assumption, is the most widely accepted for solid insulation breakdown.

In this paper, the stochastic distribution of the dielectric breakdown strength at the microscopic level is considered as the key to cause the fractal structures of the electrical trees. The distribution of the microscopic breakdown strength is assumed to obey the Weibull distribution. Iddrissu [50] has statistically measured the dielectric breakdown strength of Araldite® LY 5052 epoxy (EP) resin (cured with Aradur ® HY 5052 hardener, both supplied by Huntsman) with properly tailed test cell system. The cumulative density function (CDF) for the two-parameter Weibull distribution of the 200 μm epoxy under alternating current (AC) condition is expressed as follows [50]:

$$F(k;\alpha,\beta) = 1 - e^{-\left(\frac{k}{\alpha}\right)^{\beta}} \text{ with} \alpha = 188.72\text{kV/mm}, \beta = 15.57 \tag{24}$$

where k is the measured breakdown strength of the sample, α is the scale parameter representing the strength value corresponding to $F(k) = 63.2$ %, and β is the shape parameter representing a measure of the spread of the distribution.

To achieve the microscopic stochastic distribution of the breakdown strength in the FEA, each element is assigned with a random breakdown strength value sampled from the Weibull distribution. As the element size is quite small (micro level), a microscopic stochastic distribution can be realized. The breakdown strength of each element is given as:

$$E_b^n = \alpha \left[\ln\left(\frac{1}{1-F}\right) \right]^{\frac{1}{\beta}} \tag{25}$$

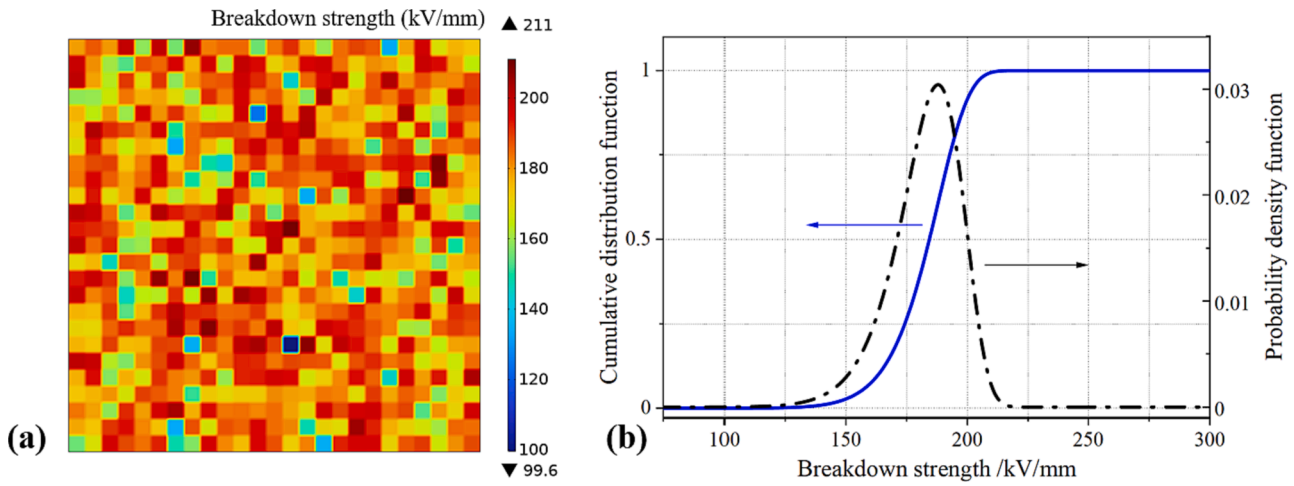

Fig. 3. Weibull distribution of the breakdown strength. (a) Spatially stochastic distribution, (b) Cumulative distribution function and probability density function of the Weibull distribution for the breakdown strength.

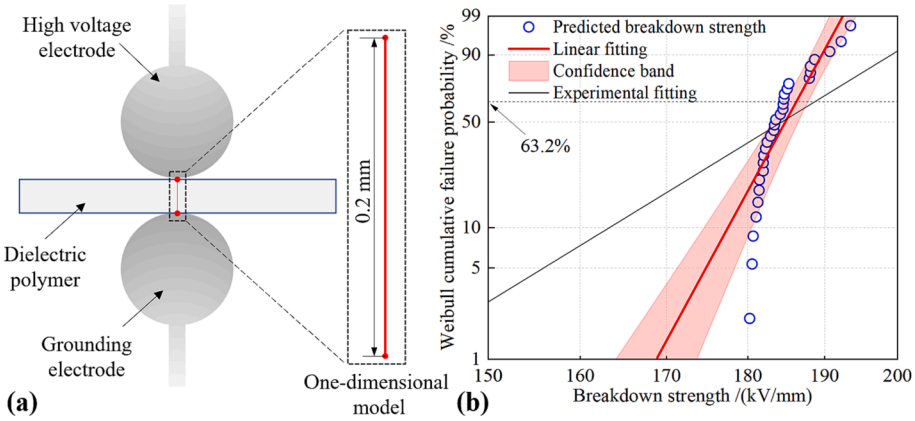

Fig. 4. Comparison of dielectric breakdown strength between numerical and experimental results. (a) Experimental setup. (b) Weibull plot.

where E_b^n is the breakdown strength of the n^{th} element, F is randomly distributed in the interval $[0,1]$, and relates to the element index n. Since F and $1-F$ follow the same probability density function (PDF), both can be denoted as the same:

$$E_b^n = \alpha\left[\ln\left(\frac{1}{F}\right)\right]^{\frac{1}{\beta}} \text{with} F = r(n,\varpi) \tag{26}$$

where $r(n,\varpi)$ is a pseudorandom function built in the COMSOL software, and ϖ is an arbitrary random seed. Fig. 3 shows the example of implementation of the stochastic Weibull distribution of dielectric strength in the finite element model.

4.2. Permittivity

Permittivity is another important material property characterizing the electric polarizability of the dielectric polymers. The dielectric frequency responses (DFR) of the epoxy resin samples (Araldite ® LY 5052 with Aradur ® HY 5052 hardener) are measured in our lab using the insulation diagnostic analyser (IDAX 300, Megger). Eight samples are fabricated and measured (see Supplementary Fig. 2). The values of 50 Hz are selected and averaged as the relative permittivity of the resin $\varepsilon_M = 3.45$, because the frequency of 50 Hz is widely used in alternating current power systems. The dielectric property of the material will degrade during the growth of electrical tree. The evolution of the permittivity is expressed in following:

$$\varepsilon(d) = \frac{\varepsilon_M}{\omega(d)+\eta} \tag{27}$$

where $\eta = 0.001$ for which the corresponding permittivity is 1000 times of its original value for the fully damaged phase [32,34]. It is also numerically tested that $\eta = 0.001$ is sufficiently small to reflect the polarization of the material.

4.3. Conductivity

The conductivity of the epoxy resin samples is also measured using the electrometer (6517B, Keithley) in our lab. The samples have an average resistivity of 236.7TΩ • cm, or a corresponding conductivity of $\sigma_M = 4.22\times10^{-13}$S • m. Similar to the permittivity, the conductivity will also degrade with the dielectric breakdown process, and the breakdown path will become conductive. The evolution of the conductivity is defined as:

$$\sigma(d) = \omega(d)\sigma_M + [1-\omega(d)]\sigma_B \tag{28}$$

where σ_B is the conductivity of the fully breakdown phase. In this paper, σ_B is taken as 4.22×10^{-10}S • m.

4.4. Fracture energy

The fracture energy of the LY 5052 epoxy resin specified in the

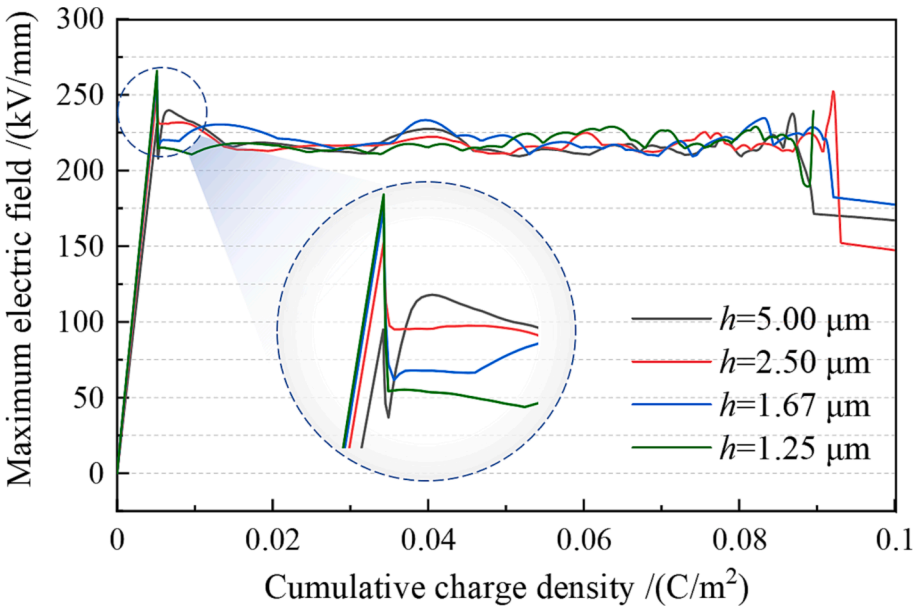

Fig. 5. The maximum electric field strength during the breakdown process of different element size h with $l = 5\mu m$.

Table 1
Comparison of computational cost of different element sizes.

l/h	$h/\mu m$	Elements	Degrees of freedom	Peak electric field/(kV/mm)
1	5	8.8×10^4	5.3×10^5	230.8
2	2.5	3.4×10^5	2.0×10^6	253.4
3	1.67	7.4×10^5	4.4×10^6	262.4
4	1.25	1.3×10^6	7.8×10^6	265.8

technical datasheet as $192 - 212\ J/m^2$, and a middle value of $G_f = 202 J/m^2$ is taken for the current study.

4.5. Length-scale parameter

Wu [46] and Tushar et al. [53] determined the length-scale based on the Griffith's theory. The Irwin's characteristic length, $l_{ch} = E_0 G_f / f_t^2$, describes the length of the fracture process zone ahead of the crack tip, with E_0 and f_t being the Young's modulus and tensile strength, respectively. Analogous to this, the internal length of the phase field model for the dielectric breakdown is modified as:

$$\overline{l_{ch}} = \frac{G_f}{\varepsilon_0 \varepsilon_r E_b^2} = 1.86 \times 10^{-4} \mathrm{m} \tag{29}$$

To ensure that the convexity of the degradation function, the length-scale parameter should satisfy $l \leq 0.85\overline{l_{ch}}$ [46]. It is also necessary to consider that $l \ll \overline{l_{ch}}$ to resolve the Γ-convergence Eq. (5). It is worth noting that the above relationship indicates that the length-scale parameter is inversely proportional to the square of the electric field strength. However, this deduction still requires further experimental validation. In this paper, the length-scale parameter is chosen as $l = 5\mu m$, and the maximum element size of $h \leq l/2$ is used for the sake of numerical robustness.

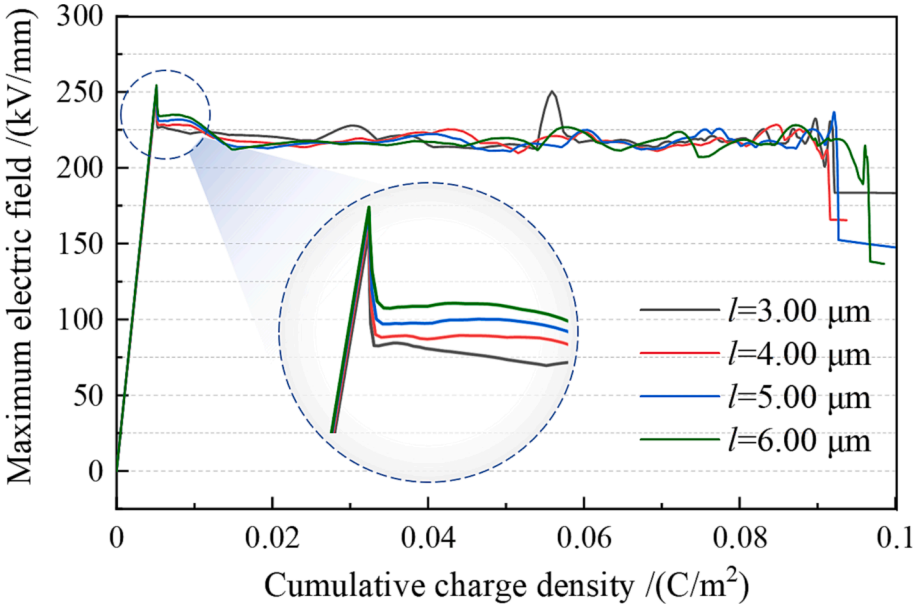

Fig. 6. The maximum electric field strength during the breakdown process of different length-scale parameter l with $h = 2.5\mu m$.

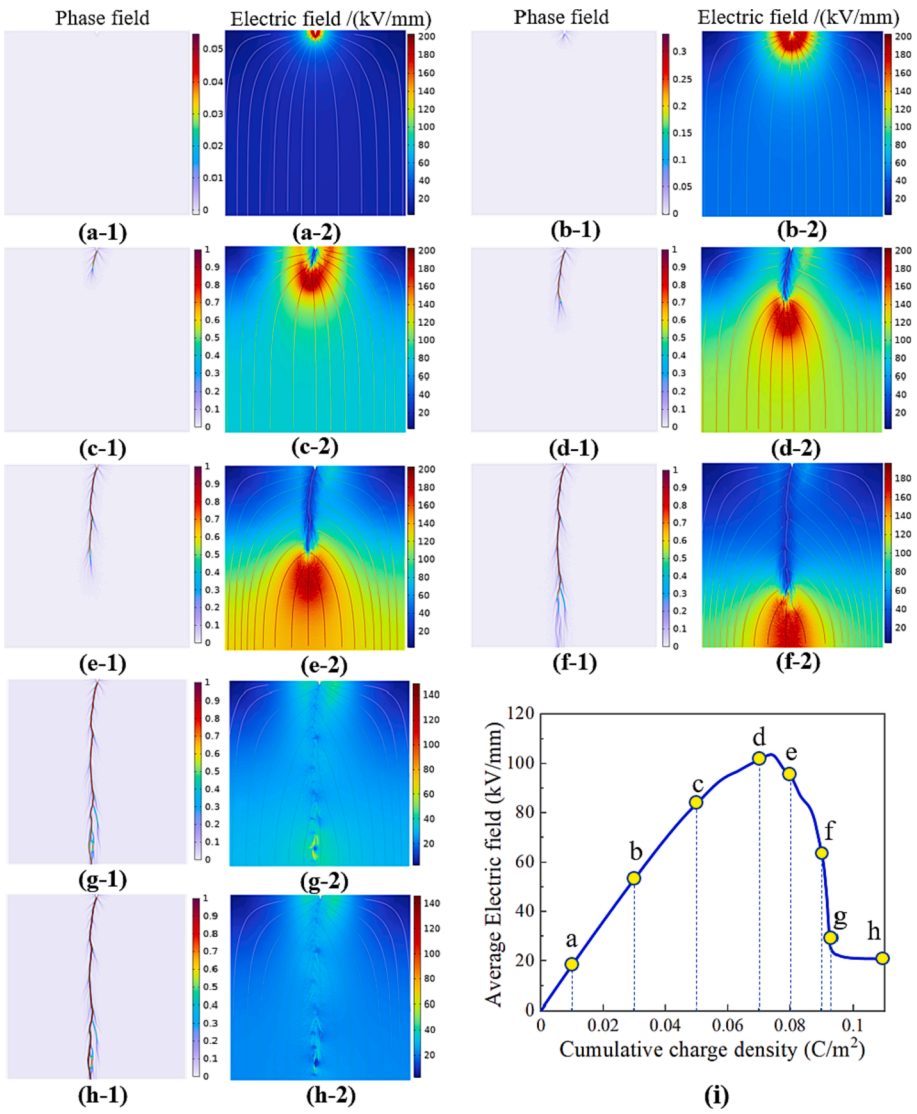

Fig. 7. Evolutions of the electrical tree and electric field during the breakdown process. (a) to (h) are eight snapshots of the breakdown path and the electric field correspond to the eight points of (i) the relationship between the average electric field and the cumulative charge density.

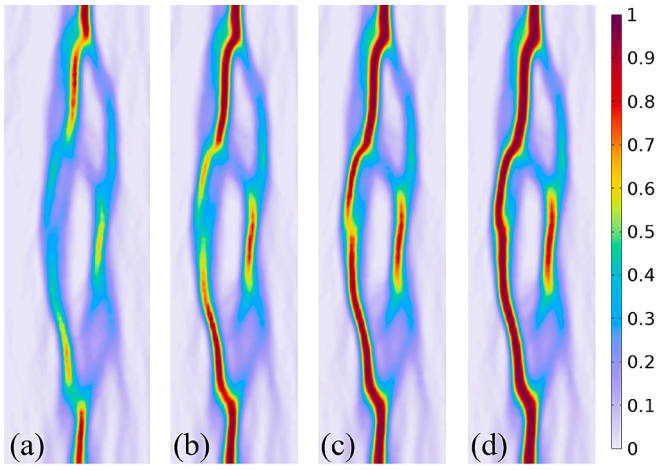

Fig. 8. The reverse growth of the electrical tree: (a) to (d) correspond to the amount of cumulative charge of 0.0920, 0.0924, 0.0927 and 0.0930C/m^2 respectively.

5. Results and discussion

5.1. Model validation

To validate the developed phase-field model, Monte Carlo simulations of dielectric breakdown were performed and compared with the experimental results [50]. The experimental setup consists of a pair of sphere electrodes and a plate epoxy sample (LY 5052) of 0.2 mm as shown in Fig. 4(a). A one-dimensional model is established to simulate the dielectric breakdown process. A ground boundary condition (BC) is applied to one side of the model, while the other side is applied with an electric potential which increases from 0 V to the fully breakdown voltage at a ramp rate of 1 kV/mm. Thirty simulations with different random seeds were conducted, and stochastic breakdown electric field strength were obtained. The Weibull statistical results are shown in Fig. 4(b), in which the calculated scale parameter and shape parameter are 186.3 kV/mm and 46.74, respectively. The experimental result, which has a scale parameter of 188.7 kV/mm, is similar to the simulated result, validating the accuracy of the model. The predicted value of the shape parameter is larger than the experimental value of 15.57, indicating that the numerical results have a smaller variation across the data set. This can be attributed to that the insufficiency of artificial

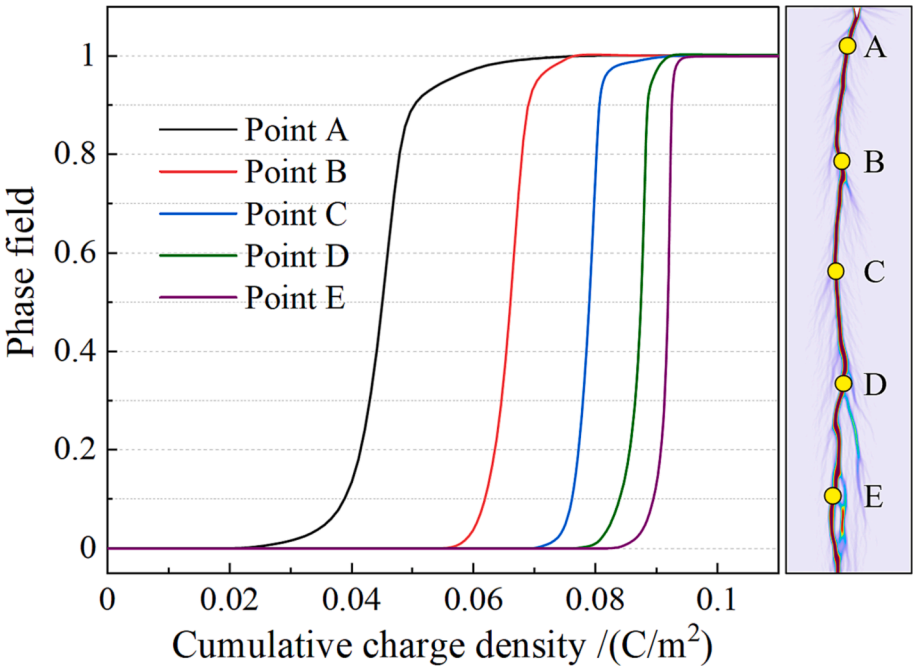

Fig. 9. The evolutions of the phase field damage variable along the breakdown path.

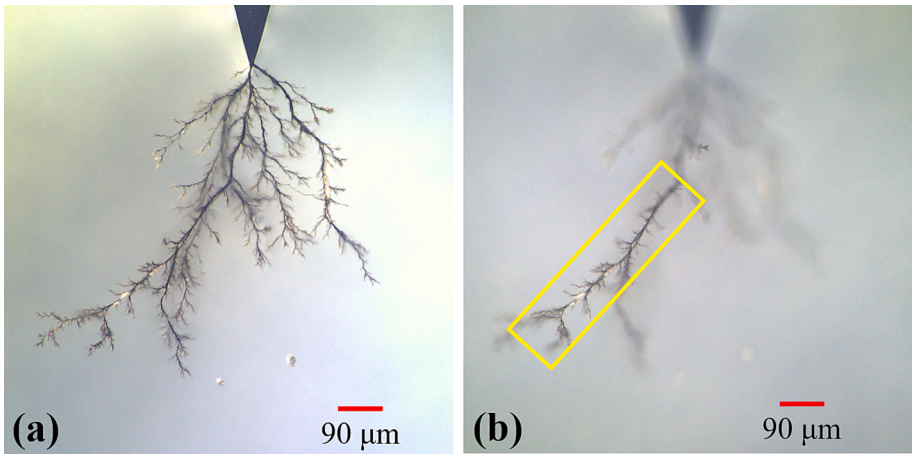

Fig. 10. Microscopic images of the electrical tree. (a) Image captured by 3D acquisition function. (b) Image captured by 2D observation.

perturbation in the simulation model, while the experimental results are susceptible to various factors, including the test conditions, environmental conditions, etc. Overall, the comparisons verified that the model can accurately predict the breakdown strength of dielectric materials and present the stochastic characteristics of breakdown strength.

5.2. Mesh sensitivity analysis

A current source is applied to the tip of the needle to simulate the charge accumulation Q, which linearly increases with time as $Q = It$, while the bottom electrode is grounded. The applied current density is 100 A/m^2. The mesh sensitivity of the phase-field model is studied by varying the element size h with a constant length-scale parameter l. The maximum electric field strength during the breakdown process of different cases is compared in Fig. 5. The results are basically consistent except for the case of $h = 5\mu m$, whose peak electric field strength is apparently lower than the other cases. This indicates that the element size h should not be greater than 2.5μm to resolve the damage regularization. However, a smaller element size will result in greater computational cost. For the case of $h = 1.25\mu m$, the simulation time is over 142 h on a Dell Precision 7560 workstation (CPU: Intel(R) i7-11800H @ 2.3 GHz; RAM: 3200 MHz 21 GB). Table 1 lists the computational cost of different cases, where the computational cost increases dramatically with the decrease of element size, while the peak electric field converges gradually.

5.3. Length-scale parameter sensitivity analysis

The most popular phase-field models, such as AT2 [19,21] and AT1 [54], are known to be length-scale parameter sensitive. In these models, the length-scale parameter is interpreted as a material property, while the Γ-convergence is neglected [55]. In contrast, the PF-CZM is length-scale parameter insensitive for brittle fracture and quasi-brittle fracture [45,53,56]. This section aims to study the length-scale parameter sensitivity of the presented model by varying the length-scale parameter l with a constant element size $h = 2.5\mu m$. The results are consistent when l varies from 3μm to 6μm, as shown in Fig. 6. The bulge of the $l = 5\mu m$ case near 0.056C/m^2 may be caused by the stochastic propagation

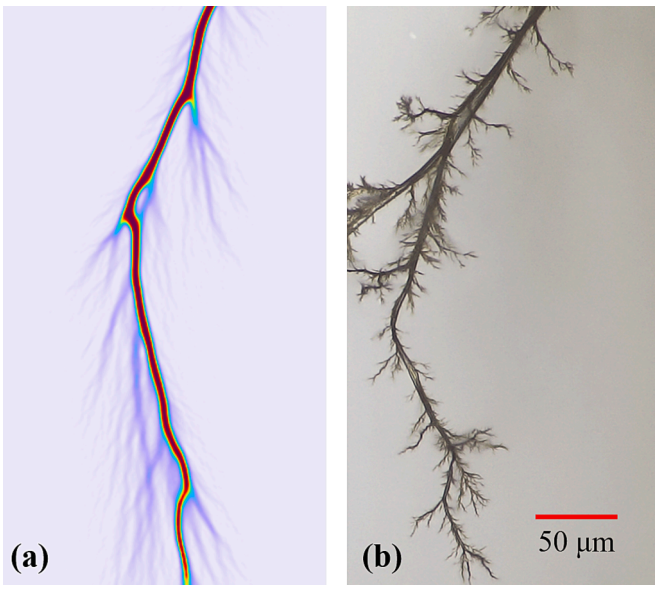

Fig. 11. Comparison of the structures of electrical trees obtained by (a) phase field simulation and (b) experimental observation.

process of the electrical trees. Except for this point, the peak electric field values are similar for the four different length-scale parameters, indicating that the presented model has inherited the length-scale parameter insensitivity of PF-CZM.

5.4. Electrical treeing process

Considering $l = 5\mu m$ and $h = 2.5\mu m$ as an example, the evolutions of the electrical tree and electric field are shown in Fig. 7. Eight snapshots corresponding to the eight points indicated in Fig. 7(g) during the breakdown process are captured. The electrical tree starts growing from the needle tip, where the electric field is the highest. Next, the primary breakdown path propagates towards the bottom electrode with multiple thin secondary paths branching towards the sides. Meanwhile, it can be observed that the electric field of the breakdown path is relatively low while the area surrounding the ends of the breakdown have a higher electric field as the material properties of the breakdown phase have degraded and the high electric field cannot be sustained. It is also found that the electrical tree has a slow initial growth followed by an accelerated propagation, until a branch reaches the bottom electrode before the branch is widened. The branch widening was also reported by Vogelsang et al. [57]. It is interesting to note that before the primary breakdown path fully bridges to the bottom electrode, a reverse breakdown path growing from the bottom electrode in the direction of the top electrode was captured before both paths meet and widened, as shown in Fig. 8. The reverse growth phenomenon was experimentally observed by Zheng et al. [58], which indicates that the presented model is able to reproduce the experimental phenomenon.

The evolutions of the phase field damage variable of five points which are vertically distributed along the breakdown path evenly are shown in Fig. 9. Similar to the tree growth model proposed by Dissado and Fothergill [59], the evolution of the phase field can be identified by three stages. In the first stage, the phase field is zero, indicating that the material is still intact. Subsequently, in the second stage, the phase field increases rapidly which correlates to the tree propagation stage. Finally, in the last stage, the growth of the phase field slows down as it approaches the value of one, staying still after which.

The simulated electrical tree has only a few main branches because the current model is two-dimensional while the electrical tree grows in 3-dimensional structures of the solid insulation. Fig. 10 shows the images of the electrical tree observed by a digital microscope (DSX1000, Olympus) in our lab. The sample was manufactured using the LY 5052 epoxy resin, and an Ogura needle was embedded in the sample whose dimensions are the same to Fig. 2. The schematic experimental setup is as shown in Supplementary Fig. 3. The electrical tree sample was immersed in a silicone oil tank to avoid the air breakdown. The high voltage source was generated by a breakdown tester (D149-DI,

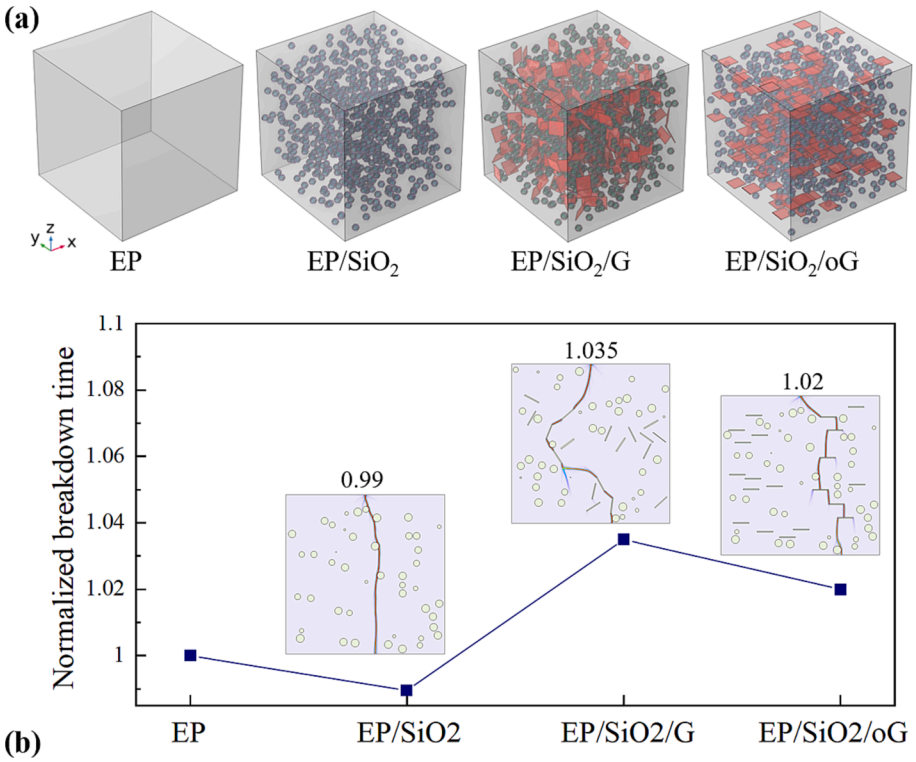

Fig. 12. Design and comparison of dielectric materials. (a) Microstructures of dielectric composites. (b) Normalized breakdown time and breakdown patterns.

HIPORONICS) and applied on the end of the Ogura needle. A digital microscope was set beside the oil tank for real-time monitoring of the electrical treeing process. After the electrical treeing, the sample was observed by the digital microscope with a higher magnification (DSX1000, Olympus) to capture the details of the electrical tree structures. Fig. 10(a) is captured by the advanced algorithms integrated in the microscope which enables the branches of different depths of field to be captured in a 2D image. However, only one main branch can be clearly captured in a conventional 2D optical observation, as shown in Fig. 11(b), which indicates that the simulated electrical treeing structure is rational for the 2D case.

With the help of the embedded random seed in the presented phase field model, Monte Carlo simulations can be carried out to obtain the random structures of the electrical tree. Fig. 11 presents the comparison of the simulated electrical tree structure and the microscopic image. The length-scale parameter $l = 6\mu m$ and the random seed $\varpi = 1000$ are taken in the simulation, while the other parameters are the same to the previous. The high similarity in the electrical treeing structures can be observed in Fig. 11. Subsequently, the fractal dimensions of the electrical trees obtained by the simulation and experiment were calculated using the image processing software Avizo 3D. The fractal dimensions of simulated and experimental electrical trees are 1.3873 and 1.3843, respectively. The excellent agreement validates the rationality of the proposed model in predicting the electrical treeing structures.

5.5. Dielectric composites design

In this section, different types of dielectric composites are designed and compared by the developed phase-field model, as shown in Fig. 12. Type 1 is a pure epoxy (EP) resin. Type 2 is an EP enhanced with silica in a volume fraction of 5 % (EP/SiO_2). Type 3 is an EP enhanced with silica sphere (5 vol%) and graphene sheet (1 vol%) (EP/SiO_2/G). Type 4 is an EP enhanced with silica sphere (5 vol%) and oriented graphene sheet (1 vol%) (EP/SiO_2/oG). For each material, a two-dimensional cross-section parallel to the YZ plane was taken to conduct the dielectric breakdown analysis. A concentrated current density source with the same magnitude was applied at the centred-top of each material, and the breakdown time was recorded. Fig. 12(b) compares the normalized breakdown time of different materials with respect to the breakdown time of the Type 1 pure EP. Using Type 1 pure EP as the baseline, Type 3 EP/SiO_2/G and Type 4 EP/SiO_2/oG has a breakdown time 3.5 % and 2 % longer than the baseline. Conversely, Type 2 EP/SiO_2 has a breakdown time 1 % shorter than the baseline. The results highlighted the positive effect of introducing graphene sheet in EP to resist dielectric breakdown. The conductive graphene sheet can "guide" the propagation of the breakdown pattern, making the breakdown path longer and thus prolonging the breakdown time.

In addition, by introducing graphene filler, the effective thermal conductivities of the dielectric composites also improved significantly. Based on the results of the finite element homogenization analysis (see Supplementary information), compared with the Type 1 pure EP, the thermal conductivities of Type 2 EP/SiO_2 and Type 3 EP/SiO_2/G increased by 10.1 % and 29.2 % respectively. The transverse thermal conductivity of Type 4 EP/SiO_2/oG (parallel to the graphene sheets) increased by 41.1 %, while the longitudinal thermal conductivity (perpendicular to the graphene sheets) increased by 12.5 %.

6. Conclusions

This paper presents a novel phase field model for simulating the electric treeing phenomenon in dielectric polymers. An advantage of the model is that all the parameters can be determined experimentally or numerically, which offers a potential to quantitatively study the breakdown mechanism of solid dielectric materials. Particularly, the microscopic stochastic dielectric breakdown strength, which is statistically measured via the Weibull distribution and embedded in the model, can be regarded as the cause of the fractal structures of the electrical tree. The analyses of mesh sensitivity and length-scale parameter sensitivity are conducted in this paper. The results show that when the mesh size is no greater than 2.5μm, the developed model is mesh-independent and length-scale parameter insensitive. The electrical tree predicted by the model exhibits a fractal shape, which has a high similarity to the morphology of the experimentally observed electrical trees.

Three types of composite materials, respectively enhanced with silica, graphene, and oriented graphene, have been designed and compared based on the developed model. The results demonstrated that the epoxy resin enhanced with 5 vol% silica and 1 vol% graphene sheet (EP/SiO_2/G) has the longest dielectric breakdown time, which is 3.5 % longer than the pure epoxy resin. Epoxy enhanced with 5 vol% silica and 1 vol% oriented graphene sheet (EP/SiO_2/oG) also has a 2 % increase in breakdown time, while the epoxy enhanced with 5 vol% silica (EP/SiO_2) decreased by 1 %. Additionally, the thermal conductivity has also been improved by introducing the graphene sheet. A maximum improvement of 41.1 % was achieved when compared with pure epoxy resin.

In a nutshell, this model provides a numerical tool to understand the breakdown mechanism of the dielectric polymers under high voltage stress, and to guide the design of dielectric composites reinforced by filler.

CRediT authorship contribution statement

Qi Wang: Conceptualization, Methodology, Formal analysis, Software, Visualization, Writing – original draft. **Yuheng Deng:** Methodology, Investigation, Validation, Investigation, Data curation, Writing – review & editing. **Malvern Yap:** Investigation, Validation, Writing – review & editing. **Yan Yang:** Methodology, Investigation, Validation, Writing – review & editing. **Jielin Ma:** Investigation, Validation, Writing – review & editing. **Wen Kwang Chern:** Resources, Project administration, Writing – review & editing. **Jin Li:** Methodology, Writing – review & editing. **Zhong Chen:** Conceptualization, Methodology, Resources, Supervision, Project administration, Funding acquisition, Writing – review & editing.

Declaration of Competing Interest

The authors declare that they have no known competing financial interests or personal relationships that could have appeared to influence the work reported in this paper.

Data availability

Data will be made available on request.

Acknowledgments

This research is supported by SP Group, the Energy Market Authority of Singapore government (under its Energy Programme EMA-EP010-SNJL-002), and Nanyang Technological University. The first author (Qi Wang) would like to thank Prof. Jian-Ying Wu and Prof. Zhong-Hui Shen for their kind comments and suggestions on the phase-field modelling.

Appendix A. Supplementary data

Supplementary data to this article can be found online at https://doi.org/10.1016/j.matdes.2023.112409.

References

[1] L. Chen, G. Msigwa, M. Yang, A.I. Osman, S. Fawzy, D.W. Rooney, P.S. Yap, Strategies to achieve a carbon neutral society: a review, Environmental Chemistry Letters (2022), https://doi.org/10.1007/s10311-022-01435-8.

[2] Z. Cai, X. Wang, L. Li, W. Hong, Electrical treeing: A phase-field model, Extreme Mechanics Letters 28 (2019) 87–95, https://doi.org/10.1016/j.eml.2019.02.006.
[3] Y. Wang, Y. Hou, Y. Deng, Effects of interfaces between adjacent layers on breakdown strength and energy density in sandwich-structured polymer composites, Composites Science and Technology 145 (2017) 71–77, https://doi.org/10.1016/j.compscitech.2017.04.003.
[4] L. Gao, Y. Yang, J. Xie, S. Zhang, J. Hu, R. Zeng, J. He, Q. Li, Q. Wang, Autonomous Self-Healing of Electrical Degradation in Dielectric Polymers Using In Situ Electroluminescence, Matter. 2 (2020) 451–463, https://doi.org/10.1016/j.matt.2019.11.012.
[5] L. Guan, L. Weng, Q. Li, X. Zhang, Z. Wu, Y. Ma, Design and preparation of ultra-thin 2D Ag-NiMOF ferroelectric nanoplatelets for PVDF based dielectric composites, Materials and Design 197 (2021), https://doi.org/10.1016/j.matdes.2020.109241.
[6] Y. Hao, Z. Feng, Z. He, J. Zhang, X. Liu, J. Qin, L. Guo, K. Bi, Gradient design of ultrasmall dielectric nanofillers for PVDF-based high energy-density composite capacitors, Materials and Design 189 (2020), https://doi.org/10.1016/j.matdes.2020.108523.
[7] L. Zhao, C. Wei, Z. Li, W. Wei, L. Jia, X. Huang, W. Ning, Z. Wang, J. Ren, High-temperature dielectric paper with high thermal conductivity and mechanical strength by engineering the aramid nanofibers and boron nitride nanotubes, Materials and Design 210 (2021), https://doi.org/10.1016/j.matdes.2021.110124.
[8] S. Yan, J.M. Jin, Three-Dimensional Time-Domain Finite-Element Simulation of Dielectric Breakdown Based on Nonlinear Conductivity Model, IEEE Transactions on Antennas and Propagation 64 (2016) 3018–3026, https://doi.org/10.1109/TAP.2016.2556699.
[9] J.M. Rodríguez-Serna, R. Albarracín-Sánchez, I. Carrillo, An improved physical-stochastic model for simulating electrical tree propagation in solid polymeric dielectrics, Polymers (basel). 12 (2020), https://doi.org/10.3390/polym12081768.
[10] Z. Lv, S. Chen, S.M. Rowland, J. Carr, T. Burnett, 3D XCT imaging of electrical tree growth in epoxy resin, IEEE Transactions on Dielectrics and Electrical Insulation. 27 (2020) 631–639, https://doi.org/10.1109/TDEI.2019.008450.
[11] Z. Lv, S.M. Rowland, S. Chen, H. Zheng, I. Iddrissu, Evolution of partial discharges during early tree propagation in epoxy resin, IEEE Transactions on Dielectrics and Electrical Insulation. 24 (2017) 2995–3003, https://doi.org/10.1109/TDEI.2017.006731.
[12] L. Niemeyer, L. Pietronero, H.J. Wiesmann, Fractal Dimension of Dielectric Breakdown, Physical Review Letters 52 (1984) 1033–1036, https://doi.org/10.1103/PhysRevLett.52.1033.
[13] L.A. Dissado, S.J. Dodd, J. v Champion, P.I. Williams, J.M. Alison,, Propagation of electrical tree structures in solid polymeric insulation, IEEE Transactions on Dielectrics and Electrical Insulation. 4 (1997) 259–279.
[14] S. Noguchi, M. Nakamichi, K. Oguni, Proposal of finite element analysis method for dielectric breakdown based on Maxwell's equations, Computer Methods in Applied Mechanics and Engineering 371 (2020), https://doi.org/10.1016/j.cma.2020.113295.
[15] Q. Wang, Y. Yang, M. Yap, W.K. Chern, Z. Chen, Simulating dielectric breakdown based on Maxwell's equations with inhomogeneous conductivity, in: 2022 IEEE Conference on Electrical Insulation and Dielectric Phenomena (CEIDP), IEEE, 2022: pp. 115–118. https://doi.org/10.1109/CEIDP55452.2022.9985246.
[16] X. Xia, B.X. Xu, X. Xiao, G.J. Weng, Modeling the dielectric breakdown strength and energy storage density of graphite-polymer composites with dielectric damage process, Materials and Design 189 (2020), https://doi.org/10.1016/j.matdes.2020.108531.
[17] E.J. Garboczi, Linear dielectric-breakdown electrostatics, Physical Review B 38 (1988) 9005–9010.
[18] A.A. Griffith, The phenomena of rupture and flow in solids, Philosophical Transactions of the Royal Society of Londres. 221 (1920) 163–198.
[19] C. Miehe, M. Hofacker, F. Welschinger, A phase field model for rate-independent crack propagation: Robust algorithmic implementation based on operator splits, Computer Methods in Applied Mechanics and Engineering 199 (2010) 2765–2778, https://doi.org/10.1016/j.cma.2010.04.011.
[20] C. Miehe, F. Welschinger, M. Hofacker, Thermodynamically consistent phase-field models of fracture: Variational principles and multi-field FE implementations, International Journal for Numerical Methods in Engineering 83 (2010) 1273–1311, https://doi.org/10.1002/nme.2861.
[21] B. Bourdin, G.A. Francfort, J.-J. Marigo, Numerical experiments in revisited brittle fracture, Journal of the Mechanics and Physics of Solids 48 (2000) 797–826. www.elsevier.com/locate/jmps.
[22] B. Bourdin, G.A. Francfort, J.-J. Marigo, The variational approach to fracture, Journal of Elasticity 91 (2008) 5–148.
[23] S. Goswami, C. Anitescu, S. Chakraborty, T. Rabczuk, Transfer learning enhanced physics informed neural network for phase-field modeling of fracture, Theoretical and Applied Fracture Mechanics. 106 (2020), https://doi.org/10.1016/j.tafmec.2019.102447.
[24] E. Samaniego, C. Anitescu, S. Goswami, V.M. Nguyen-Thanh, H. Guo, K. Hamdia, X. Zhuang, T. Rabczuk, An energy approach to the solution of partial differential equations in computational mechanics via machine learning: Concepts, implementation and applications, Computer Methods in Applied Mechanics and Engineering 362 (2020), https://doi.org/10.1016/j.cma.2019.112790.
[25] S.A. Silling, E. Askari, A meshfree method based on the peridynamic model of solid mechanics, Computers and Structures 83 (2005) 1526–1535, https://doi.org/10.1016/j.compstruc.2004.11.026.
[26] S.A. Silling, Reformulation of elasticity theory for discontinuities and long-range forces, Journal of the Mechanics and Physics of Solids 48 (2000) 175–209, https://doi.org/10.1016/S0022-5096(99)00029-0.
[27] T. Rabczuk, T. Belytschko, Cracking particles: A simplified meshfree method for arbitrary evolving cracks, International Journal for Numerical Methods in Engineering 61 (2004) 2316–2343, https://doi.org/10.1002/nme.1151.
[28] T. Rabczuk, T. Belytschko, A three-dimensional large deformation meshfree method for arbitrary evolving cracks, Computer Methods in Applied Mechanics and Engineering 196 (2007) 2777–2799, https://doi.org/10.1016/j.cma.2006.06.020.
[29] T. Rabczuk, G. Zi, S. Bordas, H. Nguyen-Xuan, A simple and robust three-dimensional cracking-particle method without enrichment, Computer Methods in Applied Mechanics and Engineering 199 (2010) 2437–2455, https://doi.org/10.1016/j.cma.2010.03.031.
[30] Z.H. Shen, J.J. Wang, J.Y. Jiang, S.X. Huang, Y.H. Lin, C.W. Nan, L.Q. Chen, Y. Shen, Phase-field modeling and machine learning of electric-thermal-mechanical breakdown of polymer-based dielectrics, Nature Communications 10 (2019), https://doi.org/10.1038/s41467-019-09874-8.
[31] Z.H. Shen, J.J. Wang, J.Y. Jiang, Y.H. Lin, C.W. Nan, L.Q. Chen, Y. Shen, Phase-Field Model of Electrothermal Breakdown in Flexible High-Temperature Nanocomposites under Extreme Conditions, Advanced Energy Materials 8 (2018), https://doi.org/10.1002/aenm.201800509.
[32] Z.H. Shen, J.J. Wang, Y. Lin, C.W. Nan, L.Q. Chen, Y. Shen, High-Throughput Phase-Field Design of High-Energy-Density Polymer Nanocomposites, Advanced Materials. 30 (2018), https://doi.org/10.1002/adma.201704380.
[33] M.X. Zhu, J.C. Li, H.G. Song, J.M. Chen, A phase field model for the propagation of electrical tree in nanocomposites, IEEE Transactions on Dielectrics and Electrical Insulation. 27 (2020) 336–342, https://doi.org/10.1109/TDEI.2019.008214.
[34] K. Chaitanya Pitike, W. Hong, Phase-field model for dielectric breakdown in solids, Journal of Applied Physics 115 (2014), https://doi.org/10.1063/1.4862929.
[35] Y. Qi, T. Xu, Y. Wang, Z. Zhang, J. Li, Simulation of Electrical Tree Breakdown Process in Epoxy Resin with Phase Field Modeling, in: 2022 IEEE Conference on Electrical Insulation and Dielectric Phenomena (CEIDP), IEEE, 2022: pp. 356–359. https://doi.org/10.1109/CEIDP55452.2022.9985345.
[36] M. Ambati, T. Gerasimov, L. de Lorenzis, A review on phase-field models of brittle fracture and a new fast hybrid formulation, Computational Mechanics 55 (2015) 383–405, https://doi.org/10.1007/s00466-014-1109-y.
[37] J.-Y. Wu, V.P. Nguyen, C.T. Nguyen, D. Sutula, S. Sinaie, S. Bordas, Phase-field modelling of fracture, Advances in Applied Mechanics. 53 (2020) (2023) 1–183, https://doi.org/10.1016/bs.aams.2019.08.001 (accessed January 16.
[38] V.P. Nguyen, T. Rabczuk, S. Bordas, M. Duflot, Meshless methods: A review and computer implementation aspects, Mathematics and Computers in Simulation 79 (2008) 763–813, https://doi.org/10.1016/j.matcom.2008.01.003.
[39] T. Rabczuk, Computational Methods for Fracture in Brittle and Quasi-Brittle Solids: State-of-the-Art Review and Future Perspectives, ISRN Applied Mathematics. 2013 (2013) 1–38, https://doi.org/10.1155/2013/849231.
[40] P. Diehl, R. Lipton, T. Wick, M. Tyagi, A comparative review of peridynamics and phase-field models for engineering fracture mechanics, Computational Mechanics 69 (2022) 1259–1293, https://doi.org/10.1007/s00466-022-02147-0.
[41] L.D. Landau, E.M. Lifshitz, Statistical Physics:, Volume 5, Elsevier, 2013.
[42] B. Bourdin, C.J. Larsen, C.L. Richardson, A time-discrete model for dynamic fracture based on crack regularization, International Journal of Fracture 168 (2011) 133–143, https://doi.org/10.1007/s10704-010-9562-x.
[43] J.-Y. Wu, V.P. Nguyen, C.T. Nguyen, D. Sutula, S. Sinaie, S. Bordas, Phase-Field Modelling of Fracture (2019).
[44] J.Y. Wu, A geometrically regularized gradient-damage model with energetic equivalence, Computer Methods in Applied Mechanics and Engineering 328 (2018) 612–637, https://doi.org/10.1016/j.cma.2017.09.027.
[45] J.Y. Wu, A unified phase-field theory for the mechanics of damage and quasi-brittle failure, Journal of the Mechanics and Physics of Solids 103 (2017) 72–99, https://doi.org/10.1016/j.jmps.2017.03.015.
[46] J.Y. Wu, Robust numerical implementation of non-standard phase-field damage models for failure in solids, Computer Methods in Applied Mechanics and Engineering 340 (2018) 767–797, https://doi.org/10.1016/j.cma.2018.06.007.
[47] A. Braides, Approximation of free-discontinuity problems, Springer Science & Business Media, Berlin, 1998.
[48] C. Kuhn, R. Müller, A continuum phase field model for fracture, Engineering Fracture Mechanics 77 (2010) 3625–3634, https://doi.org/10.1016/j.engfracmech.2010.08.009.
[49] W.X. Chen, J.Y. Wu, Phase-field cohesive zone modeling of multi-physical fracture in solids and the open-source implementation in COMSOL MULTIPHYSICS, Theoretical and Applied Fracture Mechanics. 117 (2022), https://doi.org/10.1016/j.tafmec.2021.103153.
[50] I. Iddrissu, Study of electrical strength and lifetimes of polymeric insulation for DC applications, The University of Manchester, 2017.
[51] S. Zhou, T. Rabczuk, X. Zhuang, Phase field modeling of quasi-static and dynamic crack propagation: COMSOL implementation and case studies, Advances in Engineering Software. 122 (2018) 31–49, https://doi.org/10.1016/j.advengsoft.2018.03.012.
[52] S. Zhou, X. Zhuang, H. Zhu, T. Rabczuk, Phase field modelling of crack propagation, branching and coalescence in rocks, Theoretical and Applied Fracture Mechanics. 96 (2018) 174–192, https://doi.org/10.1016/j.tafmec.2018.04.011.
[53] T.K. Mandal, A. Gupta, V.P. Nguyen, R. Chowdhury, A. de Vaucorbeil, A length scale insensitive phase field model for brittle fracture of hyperelastic solids, Engineering Fracture Mechanics 236 (2020), https://doi.org/10.1016/j.engfracmech.2020.107196.

[54] K. Pham, H. Amor, J.J. Marigo, C. Maurini, Gradient damage models and their use to approximate brittle fracture, in, International Journal of Damage Mechanics (2011) 618–652, https://doi.org/10.1177/1056789510386852.
[55] V.P. Nguyen, J.Y. Wu, Modeling dynamic fracture of solids with a phase-field regularized cohesive zone model, Computer Methods in Applied Mechanics and Engineering 340 (2018) 1000–1022, https://doi.org/10.1016/j.cma.2018.06.015.
[56] J.Y. Wu, V.P. Nguyen, A length scale insensitive phase-field damage model for brittle fracture, Journal of the Mechanics and Physics of Solids 119 (2018) 20–42, https://doi.org/10.1016/j.jmps.2018.06.006.
[57] R. Vogelsang, T. Farr, K. Fröhlich, The effect of barriers on electrical tree propagation in composite insulation materials, IEEE Transactions on Dielectrics and Electrical Insulation. 13 (2006) 373–382, https://doi.org/10.1109/TDEI.2006.1624282.
[58] H. Zheng, S.M. Rowland, I. Iddrissu, Z. Lv, Electrical treeing and reverse tree growth in an epoxy resin, IEEE Transactions on Dielectrics and Electrical Insulation. 24 (2017) 3966–3973, https://doi.org/10.1109/TDEI.2017.006729.
[59] L.A. Dissado, J.C. Fothergill, Electrical degradation and breakdown in polymers, Peter Peregrinus, London, 1992.